Geomechanics for Energy and the Environment 4 (2015) 88–99

Contents lists available at ScienceDirect

Geomechanics for Energy and the Environment

journal homepage: www.elsevier.com/locate/gete

Contact fatigue in silica sand—Observations and modeling

Zhijie Wang, Radoslaw L. Michalowski *

Department of Civil & Env. Eng., University of Michigan, Ann Arbor, MI 48109, USA

HIGHLIGHTS

- Texture of silica sand grains is rich in asperities prone to fracture when loaded.
- Delayed fracturing of grain surface features at contacts causes contact fatigue.
- An air-dry silica sand contact loaded with 2.4 N remains active for about 18 days.
- Distinct element model mimics time-dependent increase in the number of contact points within an individual inter-granular contact.

ARTICLE INFO

Article history:
Received 9 June 2015
Received in revised form 12 July 2015
Accepted 12 July 2015
Available online 20 July 2015

Keywords:
Silica sand
Sand aging
Contact fatigue
Surface texture
Contact testing
Sand grain modeling

ABSTRACT

Aging and rate effects in sand have been a subject of studies for nearly three decades, yet there is no consensus as to what the direct cause of time effects in silica sand is. A hypothesis is advocated in this paper that identifies delayed micro-fracturing of grain surface textural features at contacts as the key contributor to time effects in silica sand.

Grain-scale studies were carried out focusing on observations of time-dependent fracturing of the micro-morphological features of grain surfaces in contact, and quantitative measurements of the relative position of a grain in contact with a stainless steel plate. An apparatus was constructed that allows monitoring the time-dependent relative displacement of two grains in contact (convergence) or a grain in contact with a solid plate. Potentiometers were used to measure displacements, while a calibrated spring in one of the potentiometers was used for loading the grains with a required force. The results reveal that the rate of convergence is the largest during the period immediately after the load is applied, and the convergence continues at constant load with a decaying characteristic for about 18 days.

Simulations of grain-to-solid plate and grain-to-grain interactions were attempted using the distinct element method. The sand grain was simulated as an assembly of subparticles fused together with time- and load-dependent parallel bonds. Simulation results are consistent with the hypothesis that *contact fatigue* (or stress corrosion micro-cracking) causes a time-dependent increase in stiffness of contacts. Consequently, an increase in the macroscopic small-strain stiffness takes place, which contributes to what is often referred to as sand *aging*.

1. Introduction

Rate effects and aging in geomaterials are well documented (e.g., [1–4]), yet there is no consensus on the origin of these effects. Afifi and Woods[5] detected an increase in the shear wave velocity in silica sand subjected to prolonged loads (see also Ref. [6]), thus an increase in small strain stiffness over time. They also indicated that the increase in the shear modulus was about 2%–5% per log-cycle of time for air dry sands (after 1000 min), and the effect was more pronounced in finer sand. However, the strength of sand

* Corresponding author. Tel.: +1 734 763 2146; fax: +1 734 764 4292.
E-mail address: rlmich@umich.edu (R.L. Michalowski).

http://dx.doi.org/10.1016/j.gete.2015.07.003
2352-3808/

consolidated isotropically for different time periods was only lightly affected in tests by Daramola.[7] Delayed microfracturing of glass subjected to sustained loads was identified early by Charles[8] as a cause of time effects in glass, and he referred to it as *static fatigue*. This process was identified as a reason for deterioration of fiber optic transmission cables, and it was found to be sensitive to environmental factors, such as moisture.[9]

In the practice of geotechnical engineering the time effects have been detected in the peculiar behavior of silica sand after in-situ compaction by vibratory methods or blasting. The cone penetration resistance of freshly disturbed (compacted) sand often shows a reduction in penetration resistance immediately after compaction, but it exhibits the subsequent time-dependent increase lasting for months. Attention to this phenomenon was brought by Mitchell and Solymar,[3] who produced convincing results from a hydropower project in Nigeria, where the looser deposits were densified by using a vibro-compaction method or blasting. An early explanation of this effect identifying inter-granular bonds at contacts (precipitated mineral material), the bond breakage upon compaction, and time-dependent bond formation after the disturbance, was not confirmed by later experiments. This is not to suggest that bonds between silica sand grains do not form; they do, particularly under elevated pressure.[10] However, they have not been found to be a cause of the observed time-dependent changes in cone penetration resistance. No proposals that were suggested as explanation for this phenomenon[11,12] have been generally accepted. Another engineering consequence of the time-dependent behavior of sand was found in the behavior of piles driven into soil (*displacement piles*). The bearing capacity of the pile shaft can easily double within months after installation.[13] Time effects are also likely to play a role in operations of storage facilities for sand and other granular materials,[14,15] and operations associated with geo-energy recovery.

It was suggested by Michalowski and Nadukuru[16] that the phenomenon responsible for the observed time-dependent effects at the macroscopic scale is a process of micro-fracturing of textural features at inter-granular surfaces at contacts between grains. This process was termed *contact fatigue*, as it is similar to static fatigue in glass or rocks,[1,8] but it is confined to the region of grains in the proximity of inter-granular contacts. A justification for the contact fatigue hypothesis and the initial experimental results have been presented in Refs. [17,18]. Contact fatigue does not include cracking of entire grains, which can occur at larger stresses and can lead to the degradation of the material. The hypothesis of contact fatigue is further explored in this paper, and preliminary results are presented from tests performed using a second-generation apparatus constructed for testing individual contacts subjected to sustained loads. This paper goes beyond the hypothetical considerations presented earlier,[17] and it delivers quantitative measurements of a time-dependent relative displacement of a silica grain and a rigid plate in contact. The objective of this work is to provide further experimental evidence for static fatigue at inter-granular contacts. Also, an attempt at modeling of the fatigue process at individual contacts is presented, with a focus on the time-dependent evolution of the grain-to-grain load transfer mechanism.

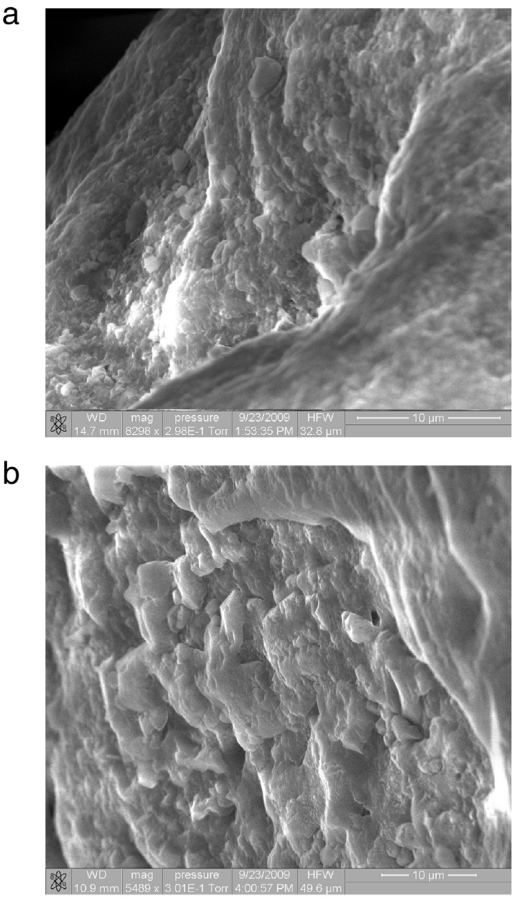

Fig. 1. Scanning electron microscope images of (a) Lake Michigan Dune sand (image width 32 μm), and (b) Ottawa sand grain (image width 48 μm).

2. Fracture kinetics

The inter-granular contacts in sand are not Hertzian contacts with well-defined geometry; instead, they are comprised of many contact sub-areas (or "contact points") with a rich surface texture, prone to fracturing upon loading.

Scanning electron microscope (SEM) images of the Lake Michigan Dune sand and Ottawa sand grain surfaces are presented in Fig. 1. When grains with such richness of surface texture come into contact and become loaded, the primary response is fracture of the microscopic asperities and mineral debris fragments. However, even after the contact force no longer increases, fracturing continues, though with a lower and decaying frequency. The physics underpinning of the delayed fracturing (static fatigue) is found in rate process theory, which takes advantage of statistical physics to define chemical and mechanical processes as a sequence of step events.

A schematic of the atomic network at a crack tip is illustrated in Fig. 2(a). The springs between atoms signify interatomic bonds (forces). The energy in the system is manifested as vibrations of atoms from their positions of equilibrium, with random amplitude in random directions, but with a well-defined frequency determined by

the Boltzmann constant, Planck constant, and the absolute temperature. The crack growth by one interatomic distance a_0 requires breaking of an interatomic bond. This is possible if the energy barrier needed to propagate the crack can be overcome.[19,20]

The portion of atoms whose energy exceeds some value $\mathscr{E}$ is given by the Maxwell–Boltzmann distribution: $\exp(-\mathscr{E}/kT)$, where kT is the energy of atoms, with k being the Boltzmann constant, and T is the absolute temperature. Hence, the cumulative distribution function is $F(\mathscr{E}) = 1 - \exp(-\mathscr{E}/kT)$, and its derivative $f(\mathscr{E}) = \exp(-\mathscr{E}/kT)/kT$ is the probability density function. Let Q be the activation energy needed to rearrange the atomic configuration, i.e., to overcome the energy barrier, Fig. 2(b). The probability (or frequency) of interatomic bond breakage can be found as

$$f_0 = \int_Q^\infty f(\mathscr{E})\, d\mathscr{E} = \int_Q^\infty \frac{e^{-\mathscr{E}/kT}}{kT}\, d\mathscr{E} = \exp\left(-\frac{Q}{kT}\right). \quad (1)$$

This is a well-known equation (e.g., Refs. [19,20]); the frequency of activation then becomes

$$\mathscr{K} = \frac{kT}{h}\exp\left(-\frac{Q}{kT}\right) \quad (2)$$

where kT/h is the frequency of atomic vibrations (h is the Planck constant). The step-wise character of the process of crack growth is illustrated in Fig. 2(b). Without any external potential, the energy barrier for crack growth is the same as that for crack healing (restoring the interatomic bond). Once the load is applied to the structure, the energy barriers for interatomic bond breaking and healing will change by amount ΔQ, Fig. 2(c), thereby changing the frequency of activation to

$$\mathscr{K}_{b,h} = \frac{kT}{h}\exp\left(-\frac{Q \mp \Delta Q}{kT}\right) \quad (3)$$

where subscripts b and h refer to bond breaking and healing (restoring), respectively; the upper sign relates to bond breaking. The net probability of overcoming the energy barrier is then $\exp(-(Q - \Delta Q)/kT) - \exp(-(Q + \Delta Q)/kT) = 2\exp(-Q/kT)\sinh(\Delta Q/kT)$, and the frequency of bond breakage becomes

$$\mathscr{K}_b = 2\frac{kT}{h}e^{-\frac{Q}{kT}}\sinh\left(\frac{\Delta Q}{kT}\right) \quad (4)$$

$\mathscr{K}_b$ is the elementary rate parameter. With much approximation, the crack tip velocity v can now be written as[19]

$$v = na_0\,\mathscr{K}_b = 2na_0\frac{kT}{h}e^{-\frac{Q}{kT}}\sinh\left(\frac{\Delta Q}{kT}\right) \quad (5)$$

where n is an integer indicating the number of interatomic distances a_0 the crack may grow in one activation step.

The purpose of this exercise was to demonstrate that there is a physical reason why delayed fracturing occurs as a discrete event at a constant load. This delayed fracturing is characteristic of *static fatigue*. When two grains come into contact, many of the microscopic features on the grain surfaces become loaded, leading to a reduction in the energy barriers for interatomic bond breaking. With a sufficiently large load, the initial fracturing will have the appearance of an instantaneous reaction, but it will be followed by a period with clearly delayed response once the load becomes stationary. This process is associated with reconfiguration of the interfaces between the micromorphological features on contacting grains, leading to *grain convergence* (grains coming closer together) and forming a firmer contact. In terms of the rate process, this is when energy portion ΔQ in Eq. (4) (associated with individual bonds) is reduced gradually, reducing the frequency of the interatomic bond breaking, and causing the process of fracture propagation or fracture initiation to decay.

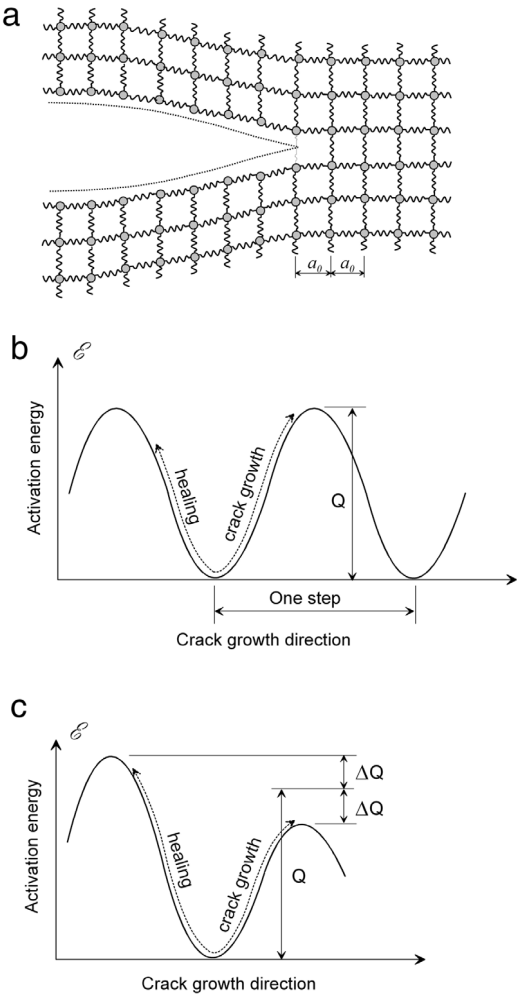

Fig. 2. Fracture kinetics: (a) schematic of the atomic network at the crack tip, (b) activation energy for crack growth and healing, and (c) change in the activation energy caused by loading.

3. Grain contact testing apparatus

Testing of individual grains and contacts is necessary for identifying the processes at the grain scale, and for gaining an insight into true interactions among grains in granular assemblies. Most tests at that scale described in the literature relate to immediate response of a grain to applied loads, i.e., deformation and crushing.[21–23] A lot

more rare are tests focused on time-dependent behavior, whether rate effects or aging. The results presented in this paper come from a particular type of test focused on the time-dependent response of a contact between a silica sand grain and a stainless steel plate subjected to sustained (constant) load. While the true contacts in granular assemblies are between two neighboring grains, such contacts cannot be easily controlled in experiments because of the evolution of the contact morphology during load application, often causing obliquity of an originally normal load. These difficulties were alluded to earlier.[21]

3.1. The apparatus

A prototype of an apparatus for testing inter-granular contacts was constructed by Nadukuru,[18,24] and a re-designed device was constructed for the purpose of testing presented in this paper. This new design is believed to eliminate some of the inaccuracies that may have been caused by the minute rotation of the moving components in the original apparatus. The schematic of the second-generation apparatus is illustrated in Fig. 3(a). Its essential portion comprises a central potentiometer (P2) with a mirror-finish stainless steel plate mounted on its rod, and a stationary reaction bracket. The grain is mounted on a standard aluminum SEM stub using a strong cyanoacrylate-based fast-acting adhesive, and the stub is mounted on the reaction bracket. The potentiometer P2 is equipped with a calibrated spring, and it is mounted on a stage that allows displacements in the direction perpendicular to the reaction bracket. Once the contact of the grain with the stainless steel plate is made, the stage is moved manually (using a micrometer screw) by a displacement needed to induce the required force that is determined by the characteristics of the calibrated spring. Subsequently, with the force at the desired magnitude, the stage is locked in place and the system is left at rest for an extended time (from days to weeks). *Convergence* is defined as the relative displacement of the stainless steel plate loading the grain and the reaction bracket on which the stub with the grain is mounted. The changes in convergence are monitored with a frequency of 1 Hz. The influence of the time-dependent convergence on the change of the force in the potentiometer spring is negligible (the measured convergence is of the order of 1 μm). Two additional potentiometers (P1 & P3, Fig. 3(a)) are mounted on the stage symmetrically on both sides of the central one (P2), with their rods resting directly against the reaction bracket. They serve as references, and are used to monitor possible deviations from symmetry during long-term testing. Ideally, during the loading process of the contact, potentiometers P1 & P3 should yield identical readings. The tolerances in the stage rails may cause deviation from symmetry (measured in nanometers), giving rise to minute rotation of the stage; in such case, convergence C is calculated as

$$C = \frac{d_1 + d_3}{2} - d_2 \tag{6}$$

where d_i ($i = 1, 2, 3$) is the displacement measured by the three potentiometers numbered as in Fig. 3(a). During the period of testing under constant load, the readings from potentiometers P1 & P3 should be constant. Preliminary tests indicated sensitivity of the measurements to changes in temperature; this sensitivity is caused by both the dependence of the contact fatigue process on temperature (Eq. (4)) and the reaction of the apparatus to thermal changes. During testing, the assembly was placed in an

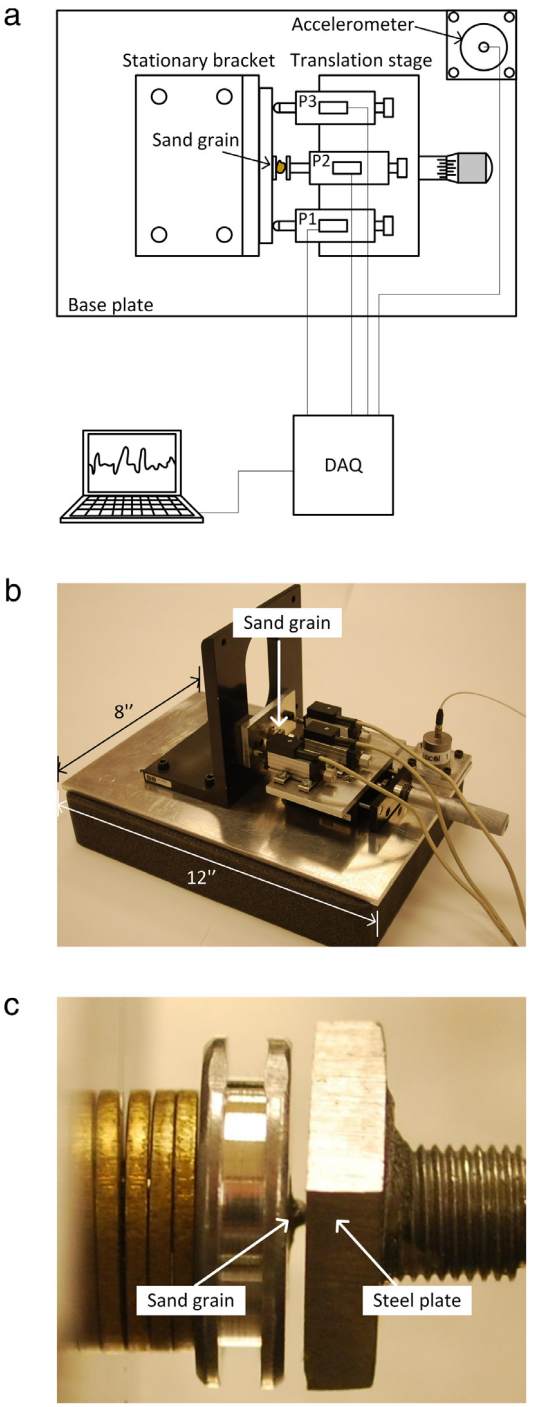

Fig. 3. Grain-scale testing apparatus: (a) schematic, (b) general view, and (c) loaded grain detail.

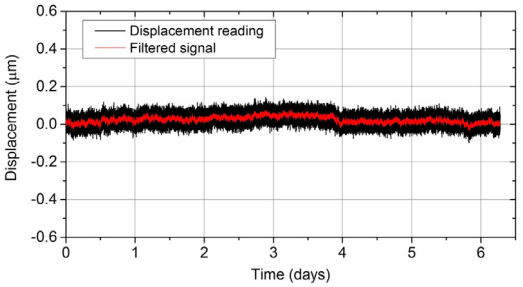

Fig. 4. Electrical signal from potentiometer P2 in the absence of silica grain (force 1.71 N).

environmental chamber and constant temperature and desired relative humidity were maintained. It was also noticed that the response of the contact is very sensitive to vibration excitations. To eliminate any disturbance caused by entering the environmental chamber, the data acquisition system was connected to a portable computer inside the chamber, and the data was periodically collected from the computer through a wireless connection.

3.2. Measurement inaccuracies

There are at least three sources of possible inaccuracies in long-term testing when using the device manufactured: mechanical, environmental, and electrical. The first type is associated with tolerances in the stage rails, and possible creep associated with rail lubricant. This was remedied by symmetrically locking the device with two screws once the desired force was applied on the contact. Inaccuracies of the second type can be caused by uncontrolled changes in temperature, humidity, and vibrations caused by external sources. Experiments were performed in an environmental chamber with controlled temperature and humidity to eliminate the first two, and a sponge-like damper was placed underneath the base of the device to reduce possible vibrations. Also, an accelerometer was installed on the device base plate to monitor vibrations with a frequency of 2 kHz. Finally, inaccuracies in measurements can be caused by instabilities in the data acquisition system. To check the stability of the electrical signal, the spring in the potentiometer was compressed to a force of 1.71 N, with the potentiometer rod pressed directly against a standard aluminum SEM stub mounted on the reaction bracket, and the signal was monitored for 6.5 days. No significant fatigue of the steel–aluminum interface was expected, and the outcome of the measurement is illustrated in Fig. 4. The signal appears to be stable, and, converted into displacement units, the noise is about 150 nm (the inner band is the signal filtered with a Savitzky–Golay filter[25]). Considering consistency of the signal, the accuracy of measurements is estimated to better than half of the band width in Fig. 4, i.e., better than ±75 nm.

4. Response of a contact to sustained load

4.1. Grain characteristics

Ottawa 20–30 sand grains were used in the tests (the numbers designate the US sieve numbers, i.e., grains were

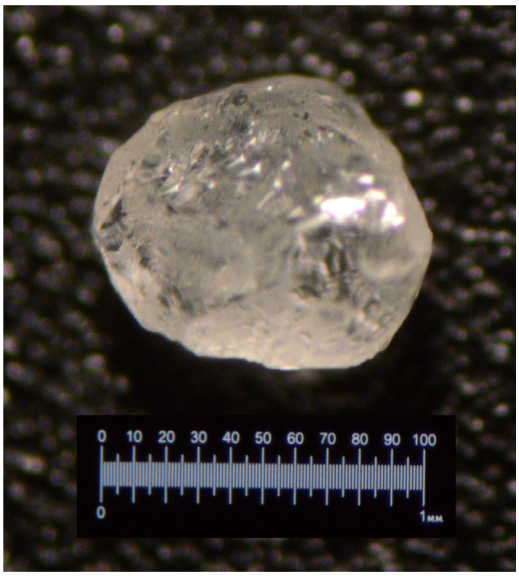

Fig. 5. Optical microscope image of Ottawa 20–30 grain.

in the sieve opening range 0.60–0.85 mm). An optical microscope image of an individual grain is shown in Fig. 5 along with a 1-mm micrometer. The surface of each sand grain tested was investigated using a scanning electron microscope (SEM). SEM images of the surface of one of the sand grains (tested later with a force of 1.25 N) are shown in Fig. 6. The first of the three images illustrates the grain mounted on a standard SEM stub using a cyanoacrylate-based fast-acting adhesive. The contour of the adhesive is clearly seen at the bottom of the image. The images in Fig. 6(b) and (c) show fragments of the grain surface of different size, indicating the richness of the surface texture at different spatial scales.

A small fragment of the surface ($30 \times 30\ \mu m$) was scanned using atomic force microscopy (AFM), and the outcome is illustrated in Fig. 7(a). Because AFM scanning results in a record of surface elevation, statistical investigation of the surface characteristics becomes possible. Fig. 7(b) illustrates the distribution of the surface elevation (roughness) of the $30 \times 30\ \mu m$ surface region. The average surface roughness S_a is measured in units of length as an average elevation of the surface features from the mean elevation

$$S_a = \frac{1}{mn}\sum_{i=1}^{m}\sum_{j=1}^{n}\left|z_{ij} - \mu\right| \tag{7}$$

where m and n are the numbers of points in the scan in the x and y directions, respectively, and z_{ij} is an elevation located by ith and jth point in the x and y-directions, respectively; μ is the average elevation

$$\mu = \frac{1}{mn}\sum_{i=1}^{m}\sum_{j=1}^{n} z_{ij}. \tag{8}$$

The $30 \times 30\ \mu m$ square fragment was relatively flat, and no compensation for the grain curvature appeared to be necessary at that scale. For the particular grain with surface texture in Fig. 7(a), the average roughness S_a was found to be 654 nm.

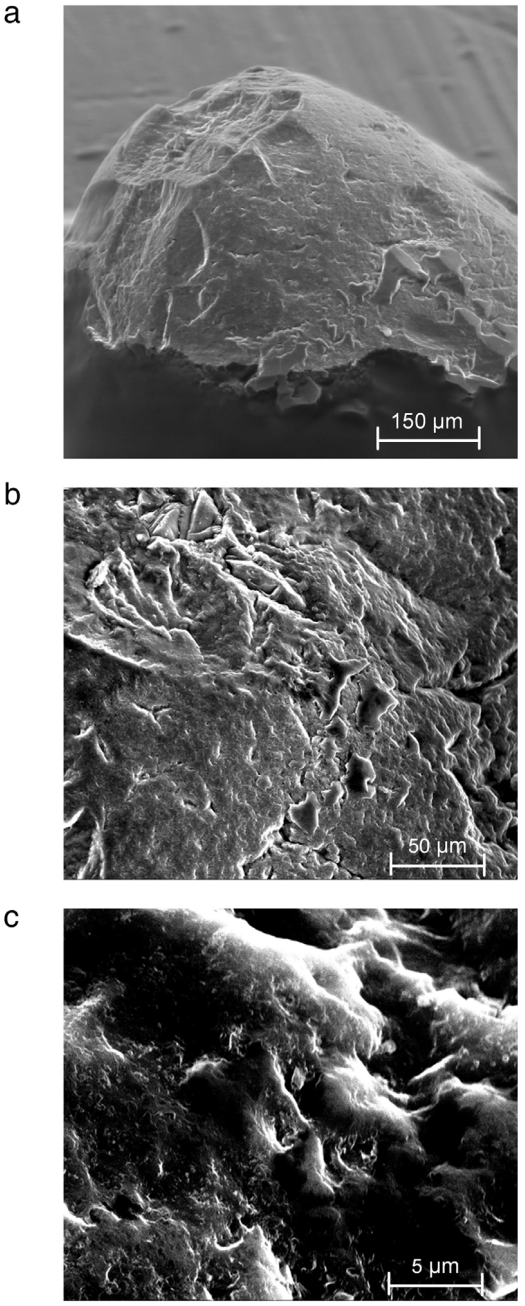

Fig. 6. SEM images of one Ottawa 20–30 grain tested: (a) grain mounted on the SEM stub with adhesive contour seen at the bottom of the image (width 650 μm), (b) fragment of the grain surface (image width 240 μm), and (c) small fragment of the surface (image width 24 μm).

4.2. Grain-to-steel plate interface tests

A typical contact between two silica sand grains has a complicated geometry. A true contact consists of many sub-contact areas (or contact "points"), and the contact plane can only be defined in a statistical sense. It was noticed in preliminary testing that even if the initial contact between two grains appeared to be fairly axi-symmetric with respect to the loading direction (visual inspection),

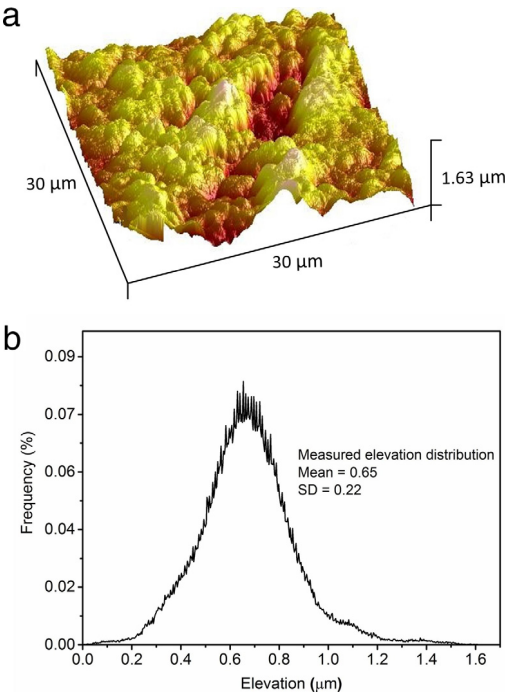

Fig. 7. Atomic force microscopy (AFM) scan: (a) a 30 × 30 μm fragment of an Ottawa sand grain surface, and (b) statistical distribution of surface elevation.

the contact would often become "progressively oblique" as the load on the contact increased and the microscopic textural features were crushed. In order to avoid this uncertainly in the load, a series of tests of grains in contact with a stainless steal plate was carried out. While such a contact cannot be considered a symmetrical half of a contact between two grains, the response of it to loading is expected to have all characteristics of a true inter-granular contact, without the uncertainty of the location of the contact plane. Results of three tests are reported here.

In each test the grain was first mounted on an aluminum stub using a strong, fast-acting adhesive so that the image of the contact area could be inspected using scanning electron microscopy. This assembly was then mounted on the reaction bracket of the apparatus, while a stainless steel plate was mounted at the end of the rod of potentiometer P2 (see Fig. 3). Then, manually using the micrometer screw on the stage, the assembly with potentiometers was moved toward the reaction bracket to make a contact of the steel plate with the grain. After the contact was established, the assembly with potentiometers was moved by the displacement required to induce the desired force (through compression of the calibrated spring in potentiometer P2). During that process the displacement was monitored using the electrical signal in the data acquisition system. Once the desired load was reached, the stage was locked in its position using two screws positioned symmetrically with respect to the loading axis (screws not shown in Fig. 3). The apparatus was then left in the environmental chamber for the predetermined time of testing, the changes in the mutual position of the grain and the reaction plate (convergence)

Table 1
Summary of grain–steel plate contact tests.

Test	Load N	Immediate convergence μm	Time-delayed convergence after 5 days nm	Average rate in the first 5 days nm/h
#1	2.40	42	680	5.70
#2	1.25	15	510	4.25
#3	0.75	4	150	1.25

were measured with a probing rate of 1 Hz, and the results were recorded on a portable computer controlling the data acquisition system.

4.3. Test results

The reports in the literature indicate sensitivity of the static fatigue process to environmental factors, such as moisture and temperature.[9] This was confirmed by the current testing. Therefore, all tests were performed in an environmental chamber, with both the temperature and the humidity controlled.

The results of three tests for three loads are presented in Fig. 8, where the mutual displacement of the grain and the reaction plate (convergence) is reported as a function of time (the data was filtered using the Savitzky–Golay filter[25]). All tests were performed at the temperature of 20 $^{\circ}C$; the relative humidity was 30% for the test with the load of 2.4 N, and 20% for the remaining tests. The test of the longest duration (22 days) was performed with a load of 2.40 N. The tests with loads of 1.25 N and 0.75 N were carried out over periods of 7.5 and 9.3 days, respectively (the test with the load of 1.25 N was terminated because of the power outage). Not surprisingly, the instantaneous displacement after load application was the largest, 42 μm, when the contact was loaded with the force of 2.40 N; it was 15 μm for the load of 1.25 N, and only 4 μm when the force of 0.75 N was applied. These results are summarized in Table 1. Similarly, the rate of convergence ranged from 5.70 to 1.25 nm/h, for the range of the high to the low force in the tests. These rates are smaller than those for grain-to-grain tests,[18] presumably because of static fatigue occurring now only on one side of the contact, and possibly due to obliquity of the load in the grain-to-grain tests in Ref. [18]. However, both types of tests indicate clearly that the process has a decaying characteristic and contact fatigue plays a significant role for about 18 days after the load is applied.

Some questions may arise regarding possible contribution of the adhesive to the measured convergence. The adhesive is likely to undergo creep under sustained load, thus it may affect the measurements of convergence. To shed some light on this issue, experiments were performed with the sand grain replaced with a stainless steel sphere (3.175 mm in diameter). It is expected that the contact fatigue at the interface of the stainless steel sphere and the stainless steel plate is insignificant, hence any changes to convergence could be attributed to time effects in the glue (creep). However, no convergence was measured beyond the noise, similar to the interface response in Fig. 4. It was concluded that the adhesive did not affect the measurements in any significant way. Also, no micro-indentation in the loading plate was detected at the grain–steel plate interface.

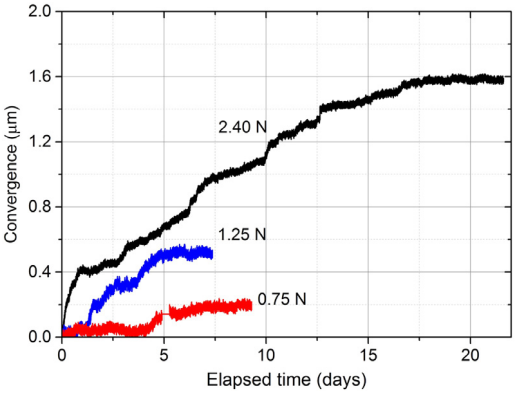

Fig. 8. Test results: grain–reaction plate convergence as a function of time.

5. Modeling of a contact

In this study of contact fatigue, physical tests are complemented by a modeling effort, so that some conceptual characteristics of the process could be numerically tested in the future before proper experiments are designed and carried out. The focus here is on the interaction of a grain with a rigid plate and on the interaction between two grains. The method used for modeling is the distinct element method. In contrast to standard applications of this method, where each distinct element simulates an individual grain, we will simulate a single grain as an assembly of bonded sub-particles, with each particle being a distinct element.

5.1. Inter-particle bond model

A numerical model of rocks was proposed by Potyondy and Cundall,[26] where the rock was simulated by densely packed particles bonded at their contacts. The chemical bonding was simulated by parallel bonds capable of transferring both forces and moments (including torsion). Deteriorating bonds in the model represent damage, and integrated over time they model damage accumulation. This model was modified by Potyondy[27] to account for time-dependency of bond damage (cracking). Forces and moments transmitted through the bonds produce tensile and compressive stresses in the bonds and the stress corrosion process is expected to take place when tension is present (particularly in the presence of moisture). This stress corrosion process is then modeled as a time-dependent reduction in bond size $\bar{D}$, Fig. 9 (Potyondy[27])

$$\frac{d\bar{D}}{dt} = \begin{cases} 0, & \bar{\sigma} < \bar{\sigma}_a \\ -\beta_1 e^{\beta_2(\bar{\sigma}/\bar{\sigma}_c)}, & \bar{\sigma}_a \le \bar{\sigma} < \bar{\sigma}_c \\ -\infty, & \bar{\sigma} \ge \bar{\sigma}_c \end{cases} \tag{9}$$

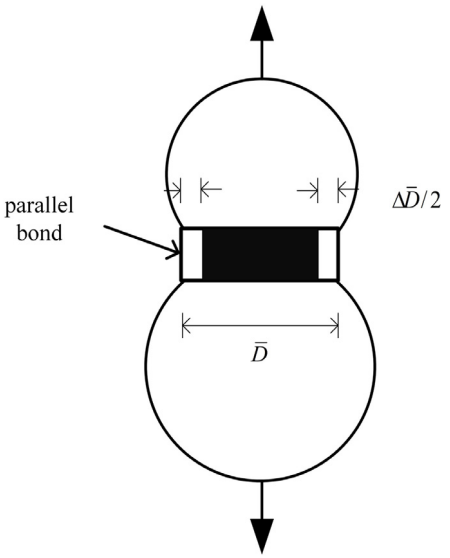

Fig. 9. Damage as a reduction in bond size $\Delta\bar{D}$ (based on Potyondy[27]).

where $\bar{\sigma}$ is the tensile stress in the parallel bond; $\bar{\sigma}_a$ is the activation stress (stress corrosion threshold); $\bar{\sigma}_c$ is the tensile strength; β_1 and β_2 are the model constants varying with temperature and chemical environment. The bar over the symbols in Eq. (9) denotes stresses in the bond. The bond can be damaged by both shear and tensile stresses. The size of the bond is shrinking in time as a result of stress corrosion, and the breakage of the bond occurs when either the shear or tensile stress reaches the limit. The bond is then removed from the contact to represent a crack. The model was named the Parallel-Bonded Stress Corrosion model (PSC), and details of it can be found in Ref. [27].

5.2. Fatigue model calibration

A model of a half of a grain in contact with a nearly-rigid plate (the plate material having Young's modulus 10 times that of the grains) is illustrated in Fig. 10. The static fatigue test with a normal force of 2.4 N (Fig. 8) was used to calibrate the PSC bond model for parameters β_1 and β_2. The model was generated using code PFC3D,[28] and parameters β_1 and β_2 were selected such that the experimental curve for load 2.4 N was approximately matched by the simulation (remaining parameters used in the simulation are listed in Table 2). The initial diameter of the bond in simulations was taken to be equal to the diameter of the smaller of the two bonded sub-particles. The model could only be roughly calibrated, as the coarse resolution of the model does not allow simulating the gradual increase of convergence; rather, the simulated function has a distinctly step-wise characteristic. The comparison of the experimental result and the simulated (calibration) curve is shown in Fig. 11.

Snapshots from the simulation of the grain loaded with a 2.4 N force (used for the purpose of calibration) are presented in Fig. 12. After the grain was loaded, the force was maintained (through a numerical servo-mechanism) for 20 days. The red and blue discs in the neighborhood of the contact in Fig. 12 indicate fractures, or bond breakage between the elements building the grain; red shows the tensile fractures and blue indicates shear debonding. There were 33 fractures immediately after the load application, Fig. 12(a); this number increased to 152 after 4 days, Fig. 12(b), and the number of cracks reached 290 after 20 days, Fig. 12(c). The final convergence, of course, matches that in the experiment since this was the calibration simulation.

Table 2
Particle contact model parameters.

Parameter	Value
Particle properties	
Young's modulus E_c	75 GPa
Average radius R_{avg}	21.1 μm
R_{avg} in refinement region	10.2 μm
$R_{\max}/R_{\min}$	1.66
Friction coefficient μ	0.5
Normal/shear stiffness ratio	2.5
Parallel bonds	
Young's modulus $\bar{E}_c$	75 GPa
Normal/shear stiffness ratio	2.5
Mean tensile strength $\bar{\sigma}_c$	300 MPa
Mean shear strength $\bar{\tau}_c$	300 MPa
Standard deviation of strengths	90 MPa
PSC parameters	
Threshold stress $\bar{\sigma}_a$	7 MPa
PSC model constant β_1	2.0×10^{-17} m/s
PSC model constant β_2	30

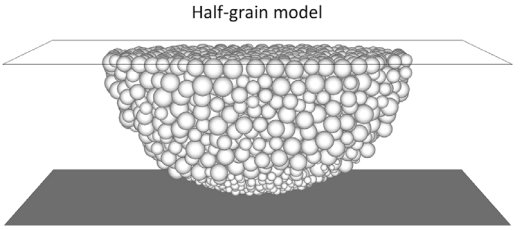

Fig. 10. Model of a half-grain in contact with a nearly-rigid smooth plate; grain radius 400 μm, 2879 spheres, average particle radius 21.1 μm in the central portion and 10.6 μm in the refined region at the contact.

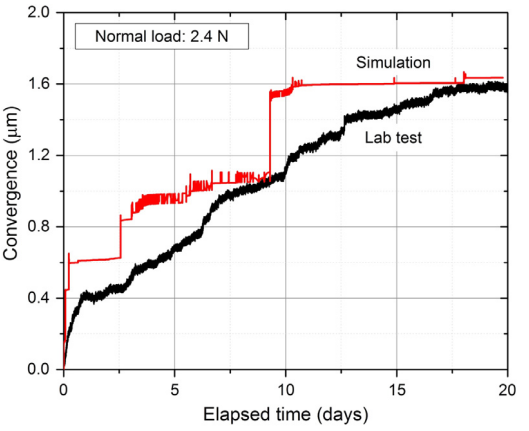

Fig. 11. Calibration simulation vs. experimental grain–steel plate convergence.

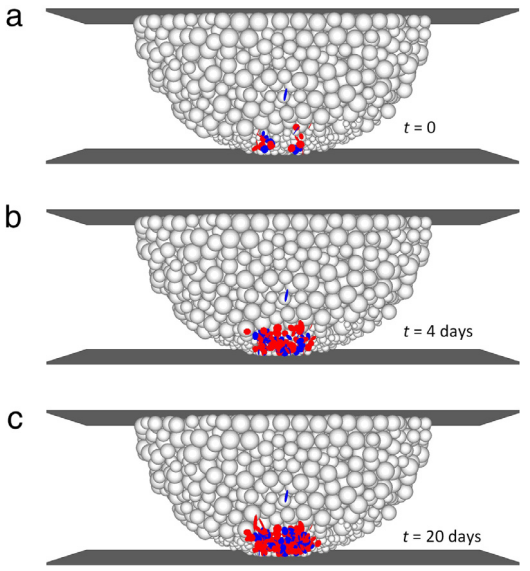

Fig. 12. Grain–steel plate contact fatigue simulation, contact force 2.4 N: (a) after application of the contact load, $t = 0$, number of cracks = 33, convergence = 0, (b) $t = 4$ days, cracks = 152, convergence = 0.93 μm, and (c) $t = 20$ days, cracks = 290, convergence = 1.64 μm. (For interpretation of the references to color in this figure, the reader is referred to the web version of this article.)

5.3. Fatigue simulation of a grain-to-grain contact

The objective of the simulation was to investigate the mechanism of load transfer from one grain to another, and to form a framework for future development of a contact law that would be appropriate for simulations of grain assemblies.

Because of computational intensity, only small regions in the immediate proximity to the contact of two grains were simulated. An inference was made that the size of the active contact region between two grains would be of the same order as a contact between two elastic spheres; the Hertz theory[29] was used to estimate the contact size (about 40 μm in diameter for grains of radius 0.4 mm, Young's modulus for quartz 72 GPa, and Poisson's ratio 0.17). The model constructed included slightly smaller regions of two grains in contact, both having a size of 30 × 30 μm in the plane parallel to the contact and 15 μm in depth, Fig. 13. The model and subsequent simulations were all developed using PFC3D code[28] with the parameters listed in Table 2. One can distinguish stresses at three different spatial scales in regard to sand: (a) average stress in the sand deposit considered as a continuum, (b) average stress in individual grains, and (c) stress at the contact region. The stress boundary conditions on the blocks in Fig. 13 were determined from the stresses measured in the simulation illustrated in Fig. 12. The horizontal confining stress on these blocks was determined to be 1.16 MPa and the vertical average stress on the upper boundary of the upper region and the lower boundary of the lower region was 12.70 MPa. These average stresses were maintained during the simulation through a numerical servo-mechanism (boundaries were assumed flexible). The observation of the

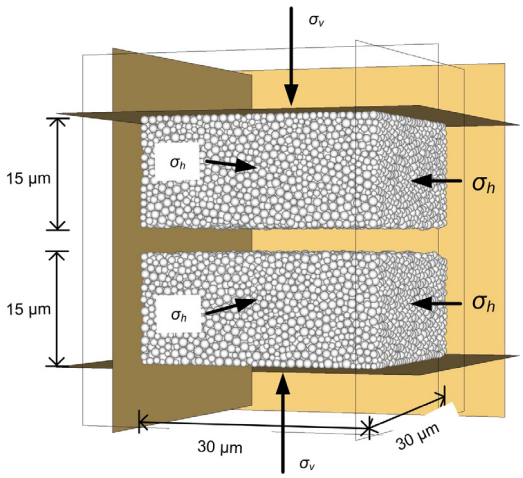

Fig. 13. Simulated contact regions of size 30 × 30 × 15 μm in upper and lower grains; 33 277 sub-particles in total, with an average radius of 0.45 μm; constant boundary load: horizontal average stress 1.16 MPa and vertical average stress 12.70 MPa (from measurements in the contact region in simulation in Fig. 12).

transmission of the load across the contact between the two blocks was the purpose of the simulation.

In order to model a realistic contact, the transmission surfaces of the lower and upper regions (contact area) were randomly generated with the goal of matching the true contact characteristics measured by atomic force microscopy and illustrated in Fig. 7(b). The Diamond-Square Algorithm[30,31] was used to generate the two surfaces in Fig. 14(a) and (b) that match the roughness characteristics in Fig. 7(b). The number of iterations used to generate the surface was 6, Hurst roughness exponent $H = 0.2$, and the elevations were scaled to match the mean elevation in AFM measurements. The comparison of the elevation distribution from the measurements and that numerically generated is illustrated in Fig. 14(c). The contact in the distinct element model was generated by carving the surfaces (removing some sub-particles) to approximately match the two that were randomly generated. To ensure a reasonable approximation, the average particle size in the model (diameter 0.90 μm) was chosen to be comparable to the size of square elements (length 0.914 μm) of the numerically generated surfaces.

The results of the simulation are presented in Fig. 15. The graphs show the force chains and the fractures occurring over time (red due to tension and blue denotes debonding caused by shear). Very weak force chains are not shown, giving an impression that some force chains terminate without reaction. The contours of the particles are not shown to preserve clarity of force chains. The three graphs show the distribution of cracks immediately after the load (shown in Fig. 13) was applied, 4 days later, and after 20 days. At time $t = 0$, there are only 10 force chains intersecting the contact, i.e., the entire load is transferred from grain to grain through ten points in the contact region. Also, there are relatively few (88) fractures at this stage, demonstrated by the small discs within the blocks simulated. The number of fractures increases twenty-fold after 4 days (1804), and there are now 18 contact "points"

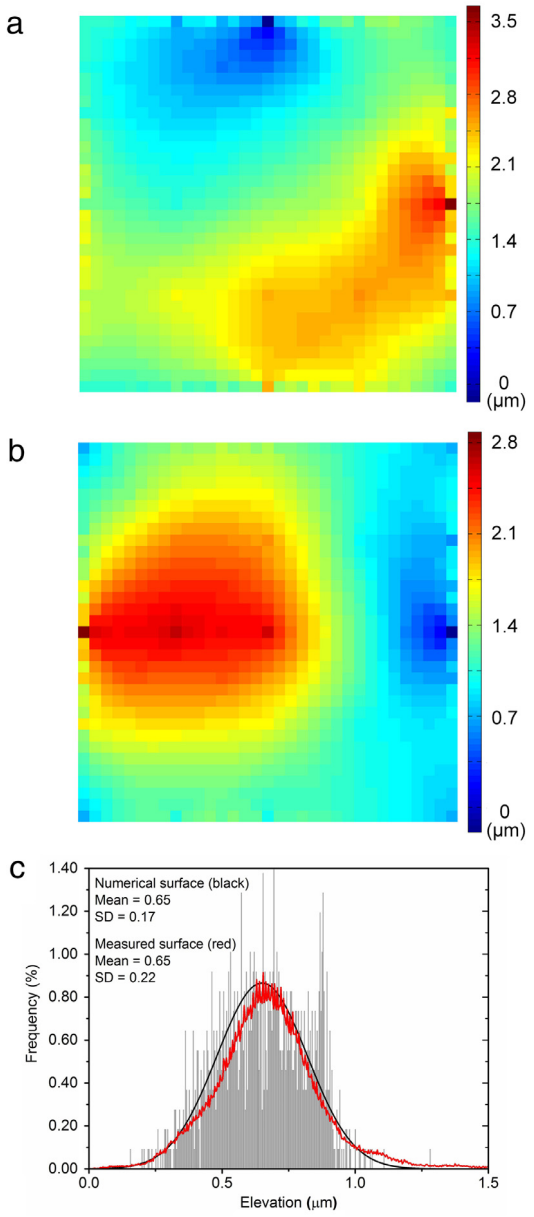

Fig. 14. Random texture generated with Diamond-Square Algorithm: (a) and (b) random texture areas of two surfaces in contact with characteristics of AFM-measured surface in Fig. 7, and (c) comparison of the elevation distributions of the numerically generated surfaces with AFM measurements.

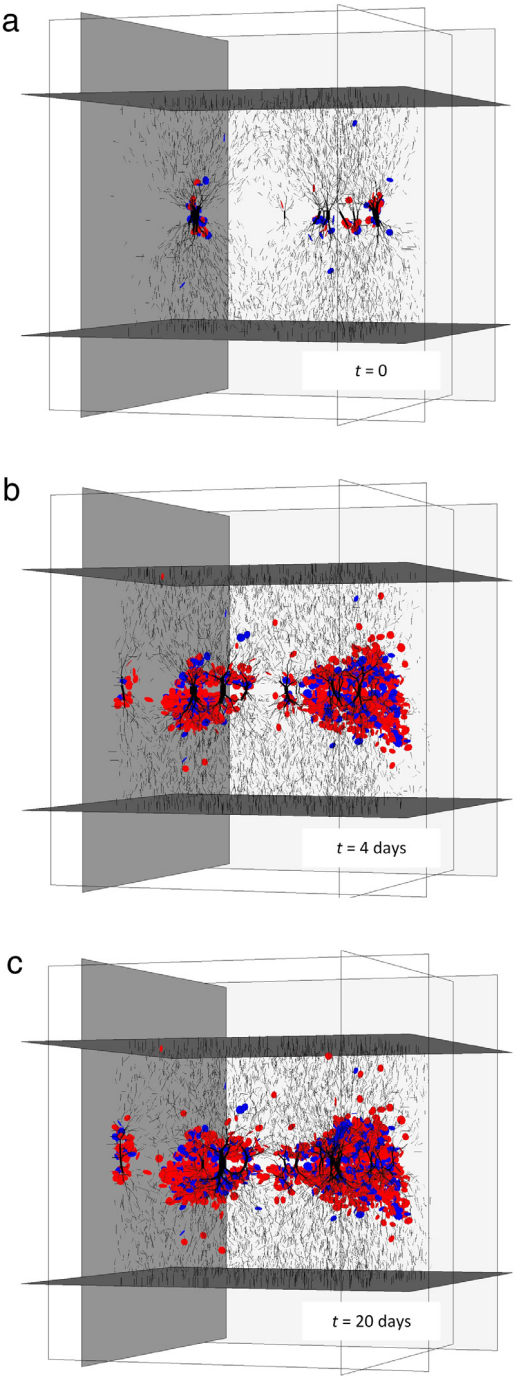

Fig. 15. Inter-granular contact simulation: force chains and crack locations, particle contours removed for clarity (refer to Fig. 13); (a) time $t = 0$ immediately after load application, 0 convergence, 10 contact points, and 88 cracks, (b) $t = 4$ days, convergence 0.24 μm, 18 contact points, and 1804 cracks, and (c) $t = 20$ days, convergence 0.27 μm, 31 contact points, and 2670 cracks. (For interpretation of the references to color in this figure, the reader is referred to the web version of this article.)

through which the load is transferred from one grain to the other. The two blocks came closer together (they converged) by 0.24 μm. Twenty days after load application, the convergence reached 0.27 μm, the number of force chains crossing the contact reached 31, and the number of bond fractures increased to 2670. The process has a decaying characteristic; there was more fracturing in the first 4 days than in the next 16 days. The convergence was now defined as the relative displacement of the upper and lower planes limiting the size of the model (Fig. 13). Notice that this convergence is significantly smaller than that in the simulation of the half-grain contact with a flat plate (Fig. 12). This is because the convergence in this simulation is an integral effect of the process in a relatively

thin region of the material as opposed to the half-grain contact problem in Fig. 12.

This simulation is consistent with earlier conjecture[17] that, with advancing static fatigue, the contacts become firmer because of the increase in the number of the contact "points", contributing to an increase in the small strain stiffness at the macroscopic scale. The latter is considered by many as one of the major consequences of sand aging.

6. Conclusions

Experiments on the behavior of silica sand contacts indicate fatigue under a condition of constant load. While substantial cracking of textural features at contacts occurs during the load application, the process of micro-cracking continues under stationary load. The contact of a silica sand grain with a stainless steel plate loaded with a force of 2.4 N displayed a *convergence* of 42 μm immediately after the load was applied, but the process continued at a constant load, with a decaying rate, to add an additional 680 nm after 5 days, and 1580 nm after 18 days. After 18 days the process could no longer be detected. The manifestation of the process seen as the grain coming closer to the plate is referred to as a *convergence*, and it is believed to be caused by delayed micro-fracturing of the morphological features at the contact (asperities, mineral debris). This time-dependent micro-fracturing is called here *static fatigue* or *contact fatigue*, and it is believed to be a key cause of silica sand aging. However, it is not suggested that contact fatigue is the only cause of aging.

A single grain was modeled as an assembly of sub-particles fused together with bonds capable of carrying forces and moments (including torsion). This bonded particle model with bonds sensitive to the stress corrosion process was used to simulate the contact regions between grains, with a focus on the time-dependent response. The distinct element model appeared to be very useful in identifying increasing time-dependent damage in the grain region adjacent to the contact. This damage is signified by fracturing of the bonds within the grain material. The consequence of this process is the readjustment of the topography of the contact that leads to a time-dependent increase in the number of contact points within an intergranular contact. This, in turn, produces an increase of the contact stiffness leading to an increase of the small-strain stiffness at the macroscopic scale. The simulation is consistent with the static fatigue hypothesis and it is consistent with the experimental outcome of tests on loaded individual grains. While some components of the model require refinements, the distinct element method has been successful in capturing the contact fatigue process.

Acknowledgments

The work presented in this paper was supported by the National Science Foundation through grants from the Civil, Mechanical and Manufacturing Innovation Program, Nos. 1129009 and 1537222. The authors also would like to thank Itasca Consulting Group for providing the PFC3D code as part of the Itasca Educational Partnership, and Dr. David O. Potyondy for his suggestions regarding the use of the Parallel-Bonded Stress Corrosion model. The scanning electron microscope and the atomic force microscope were provided by Electron Microbeam Analysis Laboratory (EMAL) of the University of Michigan supported by the National Science Foundation, Grant No. DMR-0320740, and a variety of other sources.

References

[1] Scholz CH. Mechanism of creep in brittle rock. *J Geophys Res*. 1968; 73(10):3295–3302.
[2] Hueckel T, Cassiani G, Tao F, Pellegrino A, Fioravante V. Aging of oil/gas-bearing sediments, their compressibility, and subsidence. *J Geotech Geoenviron Eng*. 2001;127(11):926–938.
[3] Mitchell JK, Solymar ZV. Time-dependent strength gain in freshly deposited or densified sand. *J Geotech Eng*. 1984;110(11):1559–1576.
[4] Lade PV, Karimpour H. Static fatigue controls particle crushing and time effects in granular materials. *Soils Found*. 2010;50(5):573–583.
[5] Afifi SS, Woods RD. Long-term pressure effects on shear modulus of soils. *ASCE J Soil Mech Found Div*. 1971;97(10):1445–1460.
[6] Anderson DG, Stokoe KH. Shear modulus: A time dependent soil property. In: *Dynamic Geotechnical Testing*. ASTM STP, vol. 654. 1978:66–90.
[7] Daramola O. Effect of consolidation age on stiffness of sand. *Géotechnique*. 1980;30(2):213–216.
[8] Charles SJ. Static fatigue of glass. I. *J Appl Phys*. 1958;29(11): 1549–1553.
[9] Cuallar E, Roberts D, Middleman L. Static fatigue lifetime of optical fibers in bending. *Fiber Integr Opt*. 1987;6(3):203–213.
[10] Guo R, Hueckel T. Silica polymer bonding of stressed silica grains: An early growth of intergranular tensile strength. *J Geomech Energy Env*. 2015;1(1):48–59.
[11] Mesri G, Feng TW, Benak JM. Postdensification penetration resistance of clean sand. *J Geotech Eng*. 1990;116(7):1095–1115.
[12] Schmertmann JH. The mechanical aging of soils. *J Geotech Eng*. 1991; 117(9):1288–1330.
[13] Jardine RJ, Standing JR, Chow FC. Some observations of the effects of time on the capacity of piles driven in sand. *Géotechnique*. 2006; 56(4):227–244.
[14] Michalowski RL. Flow of granular media through a plane parallel/converging bunker. *Chem Eng Sci*. 1987;42(11):2587–2596.
[15] Michalowski RL. Strain localization and periodic fluctuations in granular flow processes from hoppers. *Géotechnique*. 1990;40(3): 389–403.
[16] Michalowski RL, Nadukuru SS, Stress corrosion cracking and relaxation of deviatoric stress after dynamic compaction of sand. In: *37th Solid Mechanics Conference, SolMech 37, Warsaw*, September 6–11, 2010.
[17] Michalowski RL, Nadukuru SS. Static fatigue, time effects, and delayed increase in penetration resistance after dynamic compaction of sand. *J Geotech Geoenviron Eng*. 2012;138(5):564–574.
[18] Michalowski RL, Nadukuru SS, Contact fatigue: A key mechanism of time effects in silica sand. In: IS-Cambridge 2014, From Micro to Macro, K. Soga et al., ed., Cambridge, UK, September 1–3, 2014, pp. 1201–1204.
[19] Krausz AS, Krausz K. *Fracture Kinetics of Crack Growth*. Boston: Kluwer; 1988.
[20] Bažant ZP, Pang SD. Activation energy based extreme value statistics and size effect in brittle and quasibrittle fracture. *J Mech Phys Solids*. 2007;55(1):91–131.
[21] Cole DM, Mathisen LU, Hopkins MA, Knapp BR. Normal and sliding contact experiments on gneiss. *Granular Matter*. 2010;12(1):69–86.
[22] Cavarretta I, Coop M, O'Sullivan C. The influence of particle characteristics on the behaviour of coarse grained soils. *Géotechnique*. 2010;60(6):413–423.
[23] Senetakis K, Coop MR, Todisco MC. Tangential load–deflection behaviour at the contacts of soil particles. *Géotech Lett*. 2013;3(2): 59–66.
[24] Nadukuru SS. *Static fatigue: a key cause of time effects in sand* (Ph.D. thesis), Ann Arbor: University of Michigan; 2013.
[25] Savitzky A, Golay MJE. Smoothing and differentiation of data by simplified least squares procedures. *Anal Chem*. 1964;36(8): 1627–1639.
[26] Potyondy DO, Cundall PA. A bonded-particle model for rock. *Int J Rock Mech Min Sci*. 2004;41(8):1329–1364.

[27] Potyondy DO. Simulating stress corrosion with a bonded-particle model of rock. *Int J Rock Mech Min Sci*. 2007;44:677–691.
[28] PFC3D. *Particle Flow Code in 3 Dimensions (v. 4.00-201, 2013)*. Minnepolis, MN: Itasca Consulting Group, Inc.; 2008.
[29] Johnson KL. *Contact Mechanics*. Cambridge: Cambridge University Press; 1985.
[30] Kaya H, Fractal landscape generation with diamond-square algorithm. MATLAB Central File Exchange. 2013 Retrieved December 17, 2013. (http://cn.mathworks.com/matlabcentral/fileexchange/44714-fractal-landscape-generation-with-diamond-square-algorithm).
[31] Voss RF. *Random Fractal Forgeries*. Berlin: Springer; 1985.